

Cite this: *J. Mater. Chem. C*,  
2024, 12, 1675

# High-efficiency organic solar cells enabled by nonfullerene acceptors with varying alkyloxy substitution positions of the phenyl outer side chains†

Huanran Feng,<sup>‡\*</sup> Changzun Jiang,<sup>‡b</sup> Zhixiang Li,<sup>b</sup> Xiangjian Wan,<sup>‡b</sup> Bin Kan<sup>\*c</sup>  
and Yongsheng Chen<sup>‡b</sup>

Side-chain engineering has proven to be a highly effective approach in the manipulation of the molecular properties, morphology, and charge transfer/transport of non-fullerene acceptors. In addition to the alterations in branching locations and length of the alkyl side chain, a comprehensive exploration of the side chain configuration of nonfullerene acceptors (NFAs) is imperative to fully exploit their capabilities in organic solar cells (OSCs). Here, two isomeric NFAs (named *m*-BTP-OEH and *p*-BTP-OEH) with phenyl outer side chains attaching a 2-ethylhexyloxy substituent at the *meta*- or *para*-position were designed and synthesized. The effects of the alkyloxy substitution position of the phenyl outer side chains on the molecular properties, blend morphology and charge process using the polymer donor PM6 are investigated. In comparison to *p*-BTP-OEH with *para*-substitution, the *meta*-substituted side chains of *m*-BTP-OEH exhibited more favorable tilted orientations and thus better film-morphology, charge transfer/transport and reduced energy disorder when blending with PM6. As a result, the power conversion efficiency (PCE) of the devices based on *m*-BTP-OEH reached 18.02%, exhibiting a significantly enhanced fill factor (FF) of 78.41%, surpassing the photovoltaic performance of the devices based on *p*-BTP-OEH (17.63%). This study contributes to the comprehension of the significant influence of side chain configuration on the properties of molecules and its role in advancing the performance of photovoltaic systems.

Received 23rd October 2023,  
Accepted 11th December 2023

DOI: 10.1039/d3tc03864e

rsc.li/materials-c

## Introduction

The prosperity and development of organic solar cells (OSCs) exhibits their potential for next-generation photovoltaic technology with power conversion efficiencies (PCEs) surpassing 19% due to the innovations of photoactive materials.<sup>1–7</sup> Among the numerous light-harvesting materials, acceptor–donor–

acceptor (A–D–A) type non-fullerene acceptors (NFAs) contribute substantially to the performance promotion owing to their distinctive advantages of well-defined molecular structures, easier tunability of absorption and electrochemical energy levels, superior exciton dissociation and charge transport features, *etc.*<sup>8–11</sup> In particular, the best-performing devices so far are based on Y-series NFAs pairing with wide-band-gap donor polymers. Despite the great leap in efficiency of OSC devices, further improving their performance is still a key issue.<sup>12,13</sup> It is well-known that maximizing the PCE of OSCs requires simultaneously improving the three photovoltaic parameters of open-circuit voltage ( $V_{oc}$ ), short-current density ( $J_{sc}$ ) and fill factor (FF). The photovoltaic parameters are predominantly influenced by the light absorption, energy level, and morphological characteristics of the blend film, all of which can be effectively regulated through molecular engineering.<sup>14,15</sup> Thus, more efforts need to be exerted in the molecular engineering of the photoactive materials and NFAs where delicately tailored molecular structures might be designed, to build the structure–performance relationship, thereby achieving more efficient OSCs.

<sup>a</sup> Interdisciplinary Research Center of Smart Sensors, Shaanxi Key Laboratory of High-Orbits-Electron Materials and Protection Technology for Aerospace, School of Advanced Materials and Nanotechnology, Xidian University, Shaanxi, 710126, People's Republic of China. E-mail: hrfeng@xidian.edu.cn

<sup>b</sup> State Key Laboratory of Elemento-Organic Chemistry, The Centre of Nanoscale Science and Technology and Key Laboratory of Functional Polymer Materials, Institute of Polymer Chemistry, College of Chemistry, Haihe Laboratory of Sustainable Chemical Transformations, Renewable Energy Conversion and Storage Center (RECAST), Nankai University, 300071, Tianjin, China

<sup>c</sup> School of Materials Science and Engineering, National Institute for Advanced Materials, Nankai University, 300350, Tianjin, China.  
E-mail: kanbin04@nankai.edu.cn

† Electronic supplementary information (ESI) available. See DOI: <https://doi.org/10.1039/d3tc03864e>

‡ These authors contributed equally to this work.

Side chain engineering is proved to be an efficient and versatile strategy in modulating the molecular stacking and crystallinity of materials.<sup>14,16–18</sup> This approach has already been successfully applied to the high-performance Y-series NFAs, which contain inner and outer side chains respectively located on the pyrrole and thienothiophene moieties of the central fused ring.<sup>19</sup> It has been demonstrated that alterations of the alkyl chain of the inner and/or outer position can regulate the molecular interactions of the materials, thus affecting the blend morphologies and donor–acceptor compatibility, which are directly related to exciton behaviors, charge transport and material solubility.<sup>20–23</sup> For example, Yan and Zou *et al.* synthesized three molecules with different alkyl inner chain branched positions and lengths. It was found that N3 with branched and modest length of the alkyl chain exhibits better electronic properties and morphology, and thus OSC devices based on N3 exhibited the best photovoltaic performance compared to devices based on the other two molecules.<sup>24</sup> Besides the inner side chains, further studies demonstrated that the outer ones may provide a more efficient means to tailor the molecular conjugation, charge process and energy disorder, *etc.* For instance, Zou *et al.* synthesized and contrasted the NFAs with and without the outer side chains (Y11, Y18 and Y3). They found that the presence of these outer side chains resulted in a decrease in energy disorder and enhanced charge transport, through the restriction of end-group rotation.<sup>25</sup> Afterwards, Sun and Liu *et al.* reported a high-performance NFA of L8-BO with 2-butyloctyl branched outer alkyl side chains. Compared with Y6 with a linear side chain, L8-BO possesses denser molecular packing while reduced intermolecular aggregation and a resulting upshifted lowest unoccupied molecular orbital (LUMO) energy level, and thus enhanced charge transport and reduced  $E_{\text{loss}}$ , ultimately achieving higher device performance.<sup>26</sup> These studies and results have led to an increasing focus on molecular engineering on the outer alkyl chain, and demonstrate its potential on more efficient OSCs.

Furthermore, the investigation into substituting the outer side chain with a two-dimensional (2D) alkylaryl unit has now attracted much attention, which might more significantly optimize the crystallinity and aggregation properties due to its stronger steric hindrance.<sup>27–29</sup> Yan *et al.* introduced octylthienyl and hexylphenyl as outer side chains for comparison with alkyl ones. The addition of 2D side chains increased steric hindrance and slightly decreased crystallinity, leading to improved blend morphology and a resulting PCE of 17.6%.<sup>30</sup> In addition, they conducted the synthesis of three isomeric NFAs, wherein the hexyl chains were substituted at various locations on the phenyl as outer side chains. The incorporation of a *meta*-positioned hexylphenyl group, exhibiting a distinctive “tilted” orientation, has conferred upon *m*-BTP-PhC6 a heightened level of organized intermolecular arrangement, consequently leading to an augmentation in electron mobility. The optimized *m*-BTP-PhC6-based blend resulted in appropriate phase separation and improved molecular packing, leading to a significantly higher PCE of 17.7%.<sup>31</sup> Li and Wei *et al.* also carefully examined the substitution position on the thienyl

conjugated outer side chains based on two isomeric acceptors *o*-TEH and *m*-THE and the device based on *m*-THE with 2-ethylhexyl substituent at the  $\beta$ -position demonstrated an outstanding PCE of 18.51%.<sup>32</sup> These studies highlight that the location of the substituent on the 2D outer side chains has a great impact on the molecular geometry, molecular packing and furthermore the charge transport properties, and thus photovoltaic performance.

Based on the above studies, it would appear that further improvement of the OSC performance can be achieved by further molecular engineering on the outer side chains; meanwhile, a more comprehensive understanding of the structure–morphology–performance correlation can be developed. Inspired by the successful optimizations by side chains engineering mentioned above, here, two new NFAs with *meta*- and *para*-substitution of 2-ethylhexyloxy on the phenyl rings as outer side chains, namely *m*-BTP-OEH and *p*-BTP-OEH, are designed and synthesized. It was found that the side chain configurations barely affect molecule absorption, but the energy level, crystallinity and mobility were influenced, as well as the miscibility and charge transfer with the donor. Benefiting from the favorable blend morphology, charge transfer/transport dynamics and reduced energy disorder, the PM6:*m*-BTP-OEH-based devices reached 18.02% with much improved FF of 78.41% outperforming the *p*-BTP-OEH-based ones (17.63%). Our results emphasize that the location of substitution on the outer side chains has a notable impact on the photovoltaic efficiency of Y-series NFAs and show the potential of NFAs with alkyloxy substituted phenyl for higher performance OSCs.

## Results and discussion

The synthetic routes for *m*-BTP-OEH and *p*-BTP-OEH are displayed in Fig. S1, ESI.† The intermediate TPBT-2Br was synthesized according to the procedure reported by us previously without using organotin reagents.<sup>33</sup> <sup>1</sup>H NMR, <sup>13</sup>C NMR and high-resolution mass spectrometry were conducted to confirm the molecular structures (ESI†). Both isomeric NFAs demonstrate favorable solubility in typical organic solvents such as chloroform, toluene, and chlorobenzene under ambient conditions, thereby facilitating the effortless production of organic semiconductor devices.

Fig. 1b displays the UV-vis absorption spectra of the thin films of PM6, *m*-BTP-OEH and *p*-BTP-OEH, and Fig. S1 (ESI†) exhibits their solution absorption spectra. The solutions in chloroform of *m*-BTP-OEH and *p*-BTP-OEH displayed almost identical shapes of absorption curves in the range of 300–800 nm with the maximum absorption peaks at 728 and 729 nm, respectively. In the thin film state, both *m*-BTP-OEH and *p*-BTP-OEH demonstrated a significant red-shift of approximately 90 nm, accompanied by broadening, which suggests an augmentation in molecular packing within the film state. The estimation of the optical bandgap ( $E_{\text{g}}^{\text{opt}}$ ) for *m*-BTP-OEH and *p*-BTP-OEH was determined to be 1.36 eV, taking into consideration their absorption onsets. The above absorption data are

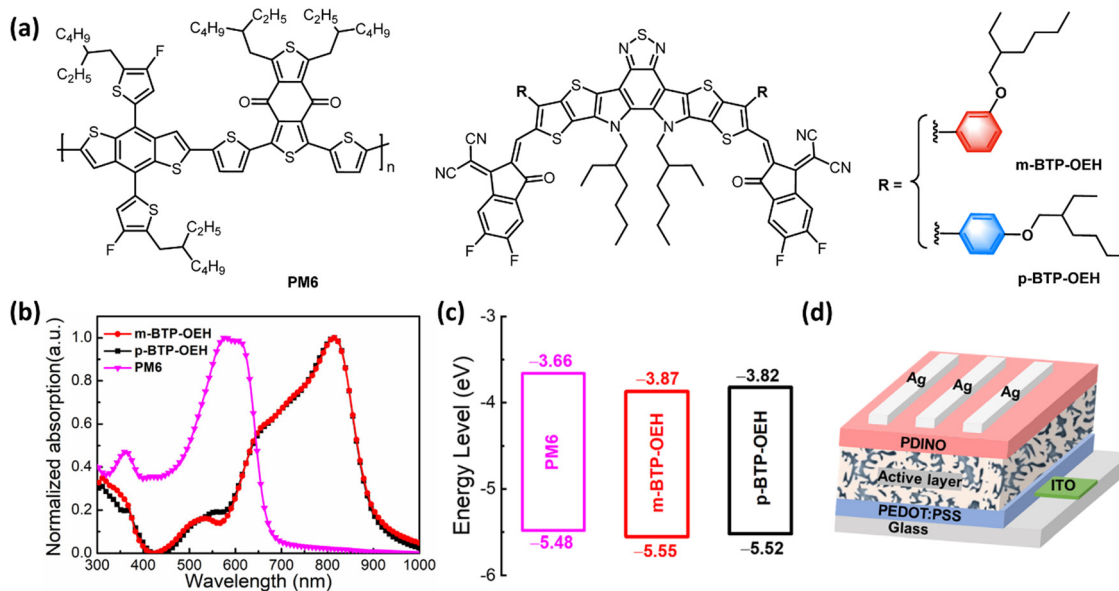


Fig. 1 (a) Chemical structures of PM6, *m*-BTP-OEH and *p*-BTP-OEH. (b) Normalized UV-vis absorption spectra of PM6, *m*-BTP-OEH and *p*-BTP-OEH in thin films. (c) Energy level alignments of the donor and acceptors. (d) Device architecture of the OSC devices.

summarized in Table 1. These results indicated that the different alkoxy-substituted positions do not have a great impact on the optical properties of *m*-BTP-OEH in comparison to that of *p*-BTP-OEH. In addition, these two molecules displayed complementary absorption with the wide bandgap polymer donor PM6, which is beneficial for the enhanced light-harvesting and thus higher  $J_{sc}$  of the corresponding OSCs.

Cyclic voltammetry (CV) was employed to estimate the frontier orbital levels of these molecules, as shown in Fig. 1c and Fig. S2 (ESI<sup>†</sup>). The highest occupied molecular orbital (HOMO)/LUMO levels obtained from the reduction/oxidation onsets of the CV curves are  $-5.55/-3.87$  and  $-5.52/-3.82$  eV for *m*-BTP-OEH and *p*-BTP-OEH, respectively. The deeper HOMO/LUMO levels of *m*-BTP-OEH might be attributed to the conjugation and inductive effects of different positions of alkoxy chain attached to the benzene ring. For *p*-BTP-OEH, substitution of the alkoxy substituent in the *para* positions on the phenyl rings would lead to a stronger conjugation effect than inductive effect. In contrast, for *m*-BTP-OEH with the *meta*-substitution, the inductive effect enhanced while the conjugation effect weakened, resulting in weakened electron donating ability of the central unit of the molecules and ultimately reduced HOMO/LUMO levels. Based on these photoelectrical properties, these two NFAs show potential for the fabrication of efficient OSC devices with the selected polymer donor PM6.

To estimate the photovoltaic properties of these two molecules with *meta*- and *para*-substituted side chains on the phenyl rings,

OSC devices were constructed using the conventional device architecture of ITO/PEDOT:PSS/active layer/PDINO/Ag, as shown in Fig. 1d. And the detailed device parameters are recorded in Tables S1–S4 (ESI<sup>†</sup>). The optimized devices based on PM6:NFA were processed with the weight ratio of 1 : 1.2 dissolved in chloroform with 0.5% 1-chloronaphthalene as a solvent additive. The devices were then subjected to thermal annealing at 100 °C for 10 min. Fig. 2a shows the current density–voltage ( $J$ - $V$ ) curves of the optimal devices and the corresponding photovoltaic parameters are listed in Table 2. The PM6:*p*-BTP-OEH-based device achieved a PCE of 17.63% with a  $V_{oc}$  of 0.884 V,  $J_{sc}$  of 26.27 mA cm<sup>-2</sup>, and FF of 75.88%. When the 2-ethylhexyloxy substituent was introduced at the *para* positions of the side chain phenyl ring, the resulting acceptor, *m*-BTP-OEH shows improved photovoltaic characteristics. Despite a drop in  $V_{oc}$ , the PCE exceeded 18% with higher  $J_{sc}$  (26.84 mA cm<sup>-2</sup>) and FF (78.41%) of the *m*-BTP-OEH-based device than that of *meta*-substituted *p*-BTP-OEH. The performance improvement primarily arises from the enhanced FF, which can be ascribed to a more efficient exciton dissociation and charge transport process, along with the diminished energetic disorder in the *m*-BTP-OEH based devices compared to the *p*-BTP-OEH based device, as elucidated in the subsequent discussion. Meanwhile, the higher  $V_{oc}$  of the *p*-BTP-OEH based device should be attributed to the high energy level and possible lower energy loss. In addition, the high performance of *m*-BTP-OEH and *p*-BTP-OEH further demonstrates that the introduction of alkoxy substituted phenyl as the outer side chain is a promising strategy for efficient acceptors.

To support the  $J_{sc}$  trend, external quantum efficiency (EQE) measurements were conducted, as displayed in Fig. 2b. Both devices demonstrate a robust photo-response within the wavelength range of 430 to 800 nm, with the maximum value of EQE nearing 90%. In addition, the *m*-BTP-OEH-based device showed slightly broader and higher photocurrent responses, thereby enhancing the  $J_{sc}$  of the corresponding devices. As a result, the

Table 1 Optical and electrochemical properties of *m*-BTP-OEH and *p*-BTP-OEH

NFAs	$\lambda_{max}^{CF}$ (nm)	$\lambda_{max}^{film}$ (nm)	$E_g^{opt}$ (eV)	$E_{HOMO}$ (eV)	$E_{LUMO}$ (eV)
<i>m</i> -BTP-OEH	729	814	1.36	-5.55	-3.87
<i>p</i> -BTP-OEH	728	814	1.36	-5.52	-3.82

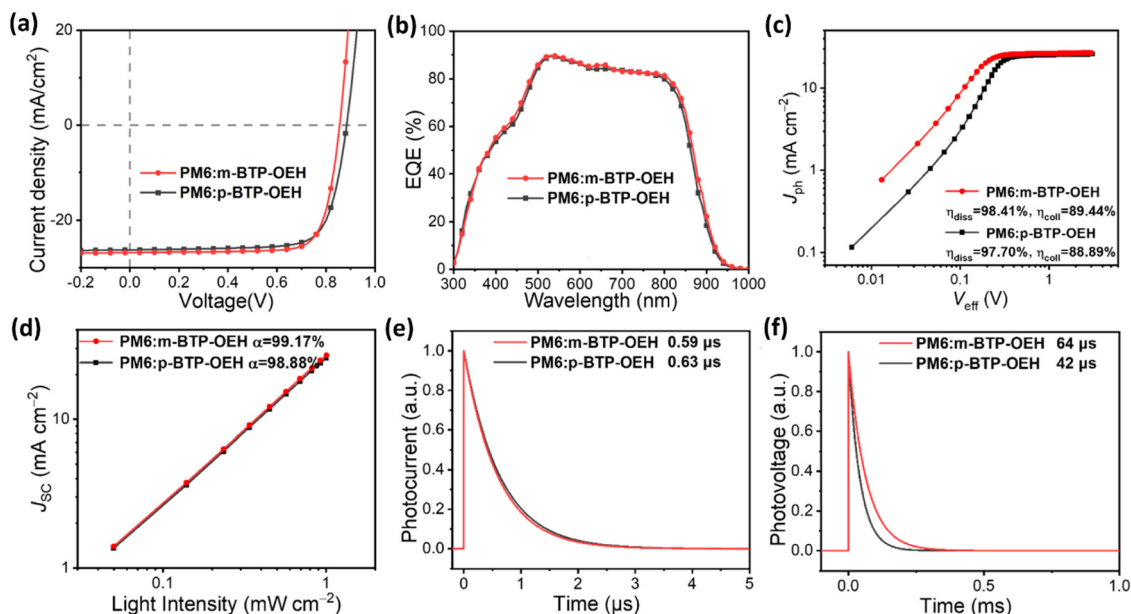


Fig. 2 (a)  $J$ - $V$  curves of the optimal devices based on PM6:*m*-BTP-OEH and PM6:*p*-BTP-OEH under AM1.5G illumination. (b) EQE curves. (c)  $J_{ph}$  versus  $V_{eff}$  and (d)  $J_{sc}$  versus light intensity of the corresponding optimized devices. (e) Transient photovoltage (TPV) and (f) transient photocurrent (TPC) of the PM6:*m*-BTP-OEH and PM6:*p*-BTP-OEH based devices.

Table 2 Optimized photovoltaic parameters of PM6:*m*-BTP-OEH and PM6:*p*-BTP-OEH systems

Active layer	$V_{oc}^a$ (V)	$J_{sc}^a$ ( $\text{mA cm}^{-2}$ )	$J_{calc}^b$ ( $\text{mA cm}^{-2}$ )	FF <sup>a</sup> (%)	PCE <sup>a</sup> (%)
PM6: <i>m</i> -BTP-OEH	0.856 (0.856 ± 0.002)	26.84 (26.94 ± 0.08)	26.00	78.41 (77.81 ± 0.29)	18.02 (17.95 ± 0.05)
PM6: <i>p</i> -BTP-OEH	0.884 (0.885 ± 0.003)	26.27 (26.10 ± 0.14)	25.49	75.88 (75.82 ± 0.39)	17.63 (17.52 ± 0.08)

<sup>a</sup> Average parameters derived from 11 independent OSCs (Tables S5 and S6, ESI). <sup>b</sup> Current densities by integrating the EQE plots.

integrated  $J_{sc}$  values obtained from the EQE curves were  $26.00 \text{ mA cm}^{-2}$  for PM6:*m*-BTP-OEH and  $25.49 \text{ mA cm}^{-2}$  for PM6:*p*-BTP-OEH, respectively, which are in line with the trend of their  $J$ - $V$  curves. The improved EQE of the *m*-BTP-OEH-based devices may be attributable to the more desirable morphology induced by *meta*-substitution, as discussed below.

To understand the reasons for the improved FF and  $J_{sc}$  of PM6:*m*-BTP-OEH in comparison with those based on PM6:*p*-BTP-OEH, we first investigated the charge carrier dynamic of these devices. As shown in Fig. 2c, the dependence of photocurrent density ( $J_{ph}$ ) on effective voltage ( $V_{eff}$ ) was measured. It is commonly postulated that the efficacy of the dissociation of photogenerated excitons and the subsequent charge collection by electrodes reach 100% under high bias conditions, specifically when the effective bias voltage ( $V_{eff}$ ) is equal to or greater than 2 V. The probability of exciton dissociation ( $P_{diss}$ ) and the efficiency of charge collection ( $P_{coll}$ ) can be determined by calculating the values of  $J_{ph}/J_{sat}$  when the system is in the short-circuit state and at maximal power output, respectively. As shown in Fig. 2c, the  $P_{diss}$  values are 98.41% and 97.91%, and the  $P_{coll}$  values are 89.44% and 88.89% for the PM6:*m*-BTP-OEH and PM6:*p*-BTP-OEH devices, respectively. The improved  $P_{diss}$  and  $P_{coll}$  demonstrate that more efficient exciton

dissociation and charge collection can be achieved in the *m*-BTP-OEH-based device, which supports the increased  $J_{sc}$  and FF. To elucidate the charge recombination mechanism, the light intensity ( $P$ ) dependence of  $J_{sc}$  was then measured. The relationship between  $J_{sc}$  and  $P_{light}$  can be explained using the formula  $J_{sc} \propto P_{light}^\alpha$ , where  $\alpha$  is the exponential factor correlated to bimolecular recombination.<sup>34,35</sup> As shown in Fig. 2d, the extracted  $\alpha$  values of PM6:*m*-BTP-OEH and PM6:*p*-BTP-OEH are 99.17%, and 98.88%, respectively. The higher  $\alpha$  value indicates reduced bimolecular recombination present in PM6:*m*-BTP-OEH-based devices.

The charge recombination dynamics of the devices were further examined through the utilization of transient photovoltage (TPV) analyses. As depicted in Fig. 2f, the TPV measurements revealed carrier lifetimes of 64 and 42  $\mu\text{s}$  for PM6:*m*-BTP-OEH and PM6:*p*-BTP-OEH-based devices, respectively, indicating weakened charge carrier recombination in the former. Transient photocurrent (TPC) decay kinetics were measured to probe the charge extraction process of these two systems. As shown in Fig. 2e, the *m*-BTP-OEH-based device showed a faster charge extraction than the *p*-BTP-OEH-based device. This observation aligns with the previously mentioned enhanced charge collection efficiency observed in the PM6:*m*-BTP-OEH system.

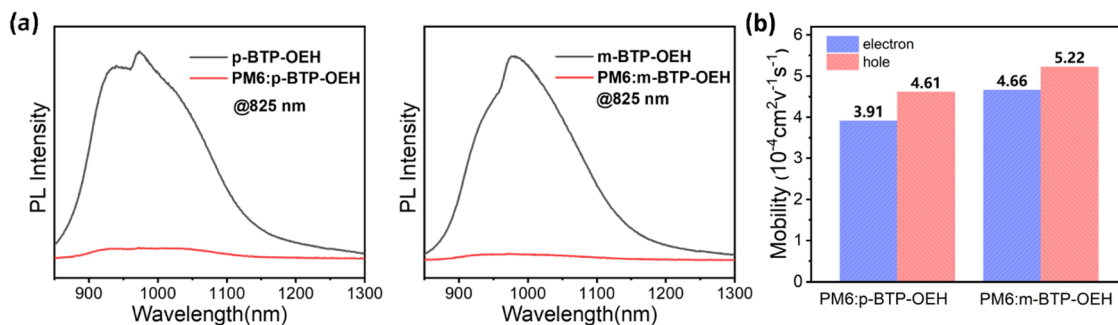


Fig. 3 (a) Photoluminescence (PL) spectra of the acceptor neat film and the blend films excited at 825 nm. (b) Histograms of the electron mobility ( $\mu_e$ ) and hole mobility ( $\mu_h$ ).

Consequently, faster carrier extraction and less charge recombination together contribute to the enhancement of FF and  $J_{sc}$ .<sup>36</sup>

Photoluminescence (PL) quenching experiments were performed to check the photo-induced exciton dissociation and charge transfer behaviors of PM6 and these two isomeric NFAs. Fig. 3b shows the PL spectra of the neat NFAs and their blend films with PM6, in which they were excited independently at 825 nm. The fluorescence quenching efficiencies for *m*-BTP-OEH and *p*-BTP-OEH in the PM6:NFA blends were determined to be 89.2% and 86.8%, respectively, indicating that more efficient charge transfer occurred in the PM6:*m*-BTP-OEH blend. The charge mobility was further evaluated by the space charge limited current (SCLC) method through fitting the dark *J*-*V* curves (Fig. 3a and Fig. S2, ESI<sup>†</sup>). The PM6:*p*-BTP-OEH system showed moderate  $\mu_h$  and  $\mu_e$  of  $4.61 \times 10^{-4}$  and  $3.91 \times 10^{-4} \text{ cm}^2 \text{ V}^{-1} \text{ s}^{-1}$ , respectively. While higher  $\mu_h$  ( $5.22 \times 10^{-4} \text{ cm}^2 \text{ V}^{-1} \text{ s}^{-1}$ ) and  $\mu_e$  ( $4.66 \times 10^{-4} \text{ cm}^2 \text{ V}^{-1} \text{ s}^{-1}$ ) are obtained in the PM6:*m*-BTP-OEH-based devices. The enhanced and more balanced charge mobilities in the PM6:*m*-BTP-OEH-based device will effectively reduce the charge accumulation in the active layer, thereby suppressing charge recombination and facilitating the charge transfer.

The morphology of the active layer is an important determinant of the corresponding device performance, to investigate the effect of side-chain orientation of NFAs on the morphology of the donor/acceptor blend, contact angle measurements were

carried out to study the miscibility and interaction between the PM6 and NFAs. As shown in Fig. 4 and Table S7 (ESI<sup>†</sup>), the surface energy ( $\gamma$ ) from the contact angles on water and glycerol was determined as  $22.0 \text{ mN m}^{-1}$ ,  $29.1 \text{ mN m}^{-1}$  and  $28.8 \text{ mN m}^{-1}$  for PM6, *m*-BTP-OEH and *p*-BTP-OEH, respectively. Then the degree of molecular miscibility was estimated by the Flory-Huggins interaction parameter  $\chi$  using the equation  $\chi_{1,2} \propto (\sqrt{\gamma_1} - \sqrt{\gamma_2})^2$ .<sup>37</sup> The  $\chi$  parameter of the PM6:*m*-BTP-OEH is 0.50, exhibiting a higher value compared to the PM6:*m*-BTP-OEH blend (0.46), suggesting lower miscibility, and thus the potential for higher domain purity in the PM6:*p*-BTP-OEH-based device. The atomic force microscopy (AFM) technique was employed to characterize the surface morphology of the blend films. Based on Fig. 6c, it is evident that both the PM6:*m*-BTP-OEH blend and the PM6:*p*-BTP-OEH blend demonstrate comparatively smooth surfaces, characterized by root-mean-square (RMS) roughness values of 0.99 nm and 0.87 nm, respectively. The larger RMS value, which is consistent with the lower miscibility between PM6 and *m*-BTP-OEH, could primarily be attributed to the stronger intermolecular stacking as discussed below.

Film morphology is also strongly dependent on the molecular packing and orientation from intrinsic structural features. Hence, to explore the impact of the side-chain configurations on molecular packing, the crystalline properties were evaluated by grazing-incidence wide-angle X-ray scattering (GIWAXS). As shown in Fig. 5a and b, both these NFA neat

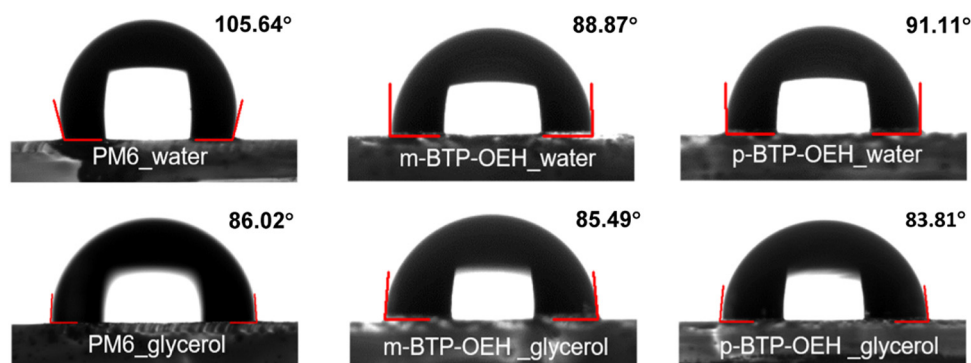


Fig. 4 Contact angle of neat PM6, *m*-BTP-OEH and *p*-BTP-OEH films with water and glycerol droplets.

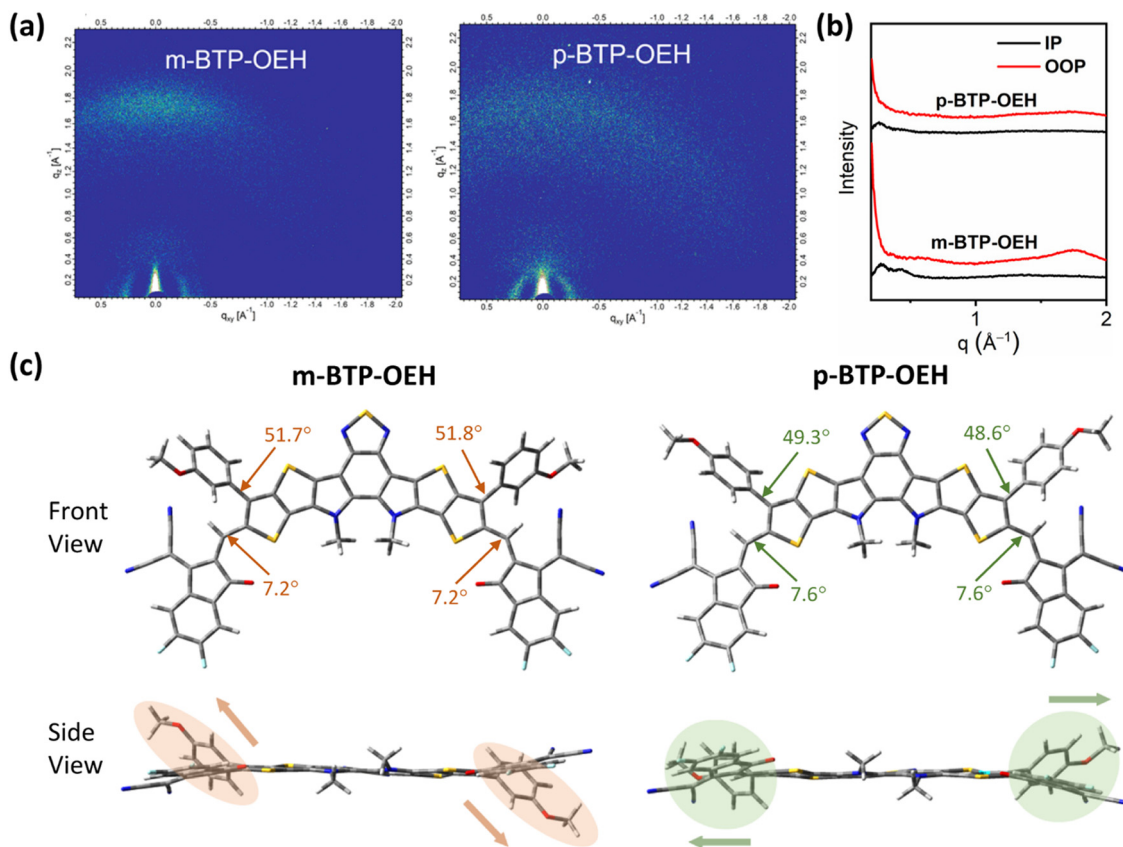


Fig. 5 (a) 2D GIWAXS patterns and (b) corresponding 1D scattering profiles along the in-plane and out-of-plane directions for *m*-BTP-OEH and *p*-BTP-OEH. (c) DFT calculations of the optimized molecular geometry.

films as cast present dominantly face-on oriented  $\pi$ - $\pi$  stacking; moreover, *m*-BTP-OEH exhibited pronounced (010)  $\pi$ - $\pi$  stacking diffraction compared to *p*-BTP-OEH due to the *meta*-substituted side chains. The  $\pi$ - $\pi$  stacking diffraction (010)

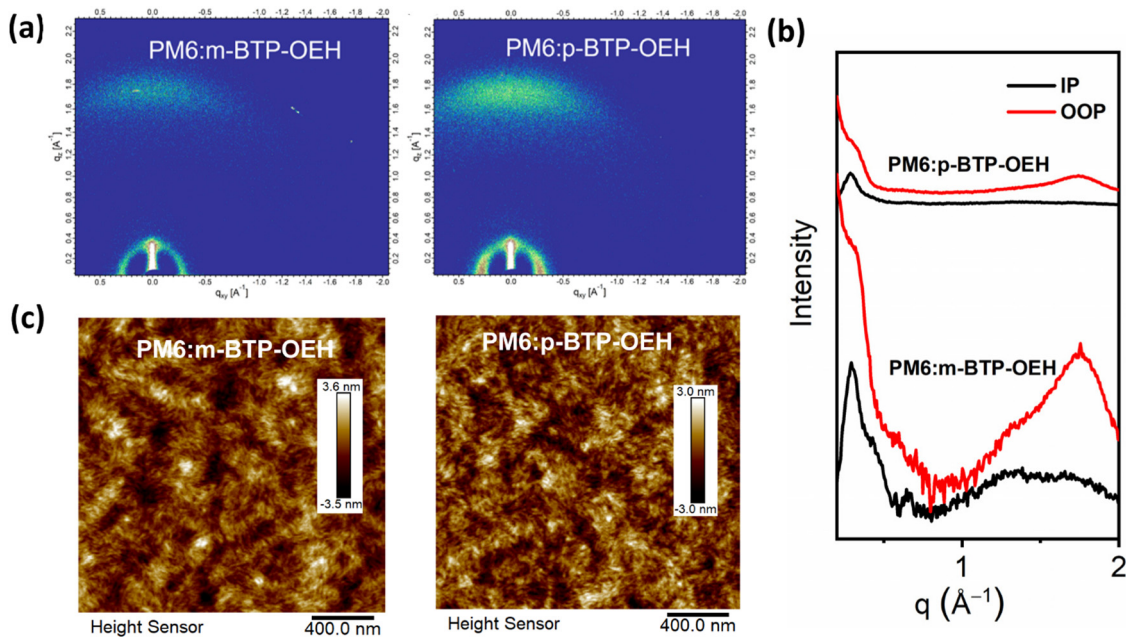


Fig. 6 (a) 2D GIWAXS patterns and (b) corresponding 1D scattering profiles along the in-plane and out-of-plane directions for PM6:*m*-BTP-OEH and PM6:*p*-BTP-OEH. (c) AFM height images.

peaks of *m*-BTP-OEH and *p*-BTP-OEH locate at 1.74 and 1.70 Å<sup>-1</sup> in the OOP direction and these peaks correspond to the  $\pi$ - $\pi$  stacking distance of 3.61 and 3.69 Å, respectively. The closer packing along with stronger stacking diffraction of *m*-BTP-OEH could be favorable for charge transport. Meanwhile, the molecular geometries of these two NFAs were calculated by density-functional theory (DFT) calculations to get insights into the effects of side chain configuration on intermolecular packing. As shown in Fig. 5c, the side chains of *m*-BTP-OEH adopted tilted orientations, which will favor intermolecular packing, despite the larger dihedral angles in its molecular geometry than those of *p*-BTP-OEH.<sup>31,38</sup>

Then, the blend films of NFAs with PM6 under the optimized condition are also characterized by GIWAXS, respectively (Fig. 6a and b). The face-on orientation of both acceptors and PM6 remained predominant following their blending. The PM6:*p*-BTP-OEH blended film exhibits (100) lamellar peaks at 0.29 Å<sup>-1</sup> along the IP direction with a crystal coherence length (CCL) of 16.10 Å. In comparison, the PM6:*m*-BTP-OEH displays (100) lamellar peaks at 0.30 Å<sup>-1</sup> with CCL of 17.89 Å. The diffraction peak associated with  $\pi$ - $\pi$  stacking in the PM6:*m*-BTP-OEH blended film is observed at 1.75 Å<sup>-1</sup> corresponding to a *d*-spacing of 3.58 Å, whereas the PM6:*p*-BTP-OEH blended film possesses a  $\pi$ - $\pi$  stacking peak at 1.74 Å<sup>-1</sup> with a corresponding *d*-spacing of 3.61 Å. The shorter *d*-spacing and longer CCL values imply that the PM6:*m*-BTP-OEH blended films have higher crystallinity than those of PM6:*p*-BTP-OEH, consistent with its higher mobilities. Moreover, the more ordered molecular packings in the PM6:*m*-BTP-OEH blend suggests lower energy disorders. According to the discussions in recent reports, the measurement of Urbach energy ( $E_U$ ) can serve as an indicator of the extent of energy disorder in a system.<sup>39-42</sup> Thus, the FTPS-EQE were analyzed to determine  $E_U$  for these two systems. As shown in Fig. S4 (ESI<sup>†</sup>), the  $E_U$  of the PM6:*m*-BTP-OEH blend is 21.82 meV, lower than value of the PM6:*p*-BTP-OEH blend (23.85 meV), which agrees with the higher crystallinity and thus better charge transport of PM6:*m*-BTP-OEH-based devices.

## Conclusion

In summary, two Y6 derivatives named *m*-BTP-OEH and *p*-BTP-OEH were developed by attaching a 2-ethylhexyloxy substituent at the *meta*- or *para*-position of the phenyl side chain for high-performance OSCs. By exploration of the correlation between the structure of the molecule and the device performance, it was found that the absorption of the molecules is barely affected by the side chain configurations, but the energy level, crystallinity and mobility were influenced, as well as the miscibility and charge transfer with the polymer donor PM6. In comparison to *p*-BTP-OEH with *para*-substitution, the *meta*-substituted side chains of *m*-BTP-OEH provided more favorable tilted orientations and thus better film-morphology, charge transfer/transport dynamics and reduced energy disorder when blending with PM6. Thus, the PCE of the *m*-BTP-OEH-based

devices achieved a value of 18.02%, accompanied by a  $V_{oc}$  of 0.856 V,  $J_{sc}$  of 26.84 mA cm<sup>-2</sup>, and FF of 78.41%. These results surpass the performance of the *p*-BTP-OEH-based devices, which exhibited a PCE of 17.63%. This work demonstrates that subtly optimizing the side-chain configuration is an effective strategy to gently modify the molecular properties, morphology, and charge processes of the NFAs, as well as proving the potential of NFAs with alkyloxy substituted phenyl groups for higher performance OSCs.

## Conflicts of interest

The authors declare no conflict of interest.

## Acknowledgements

The authors gratefully acknowledge the financial support from the MoST of China (2022YFB4200400, 2019YFA0705900) and NSFC (22005234, 21935007, 52025033, 52303237). The authors thank Yu Chen at the Beijing Synchrotron Radiation Facility, Institute of High Energy Physics for performing GIWAXS measurements.

## References

- 1 T. Chen, S. Li, Y. Li, Z. Chen, H. Wu, Y. Lin, Y. Gao, M. Wang, G. Ding, J. Min, Z. Ma, H. Zhu, L. Zuo and H. Chen, *Adv. Mater.*, 2023, **35**, 2300400.
- 2 L. Zhu, M. Zhang, J. Q. Xu, C. Li, J. Yan, G. Q. Zhou, W. K. Zhong, T. Y. Hao, J. L. Song, X. N. Xue, Z. C. Zhou, R. Zeng, H. M. Zhu, C. C. Chen, R. C. I. MacKenzie, Y. C. Zou, J. Nelson, Y. M. Zhang, Y. M. Sun and F. Liu, *Nat. Mater.*, 2022, **21**, 656-663.
- 3 W. Gao, F. Qi, Z. Peng, F. R. Lin, K. Jiang, C. Zhong, W. Kaminsky, Z. Guan, C. S. Lee, T. J. Marks, H. Ade and A. K. Jen, *Adv. Mater.*, 2022, **32**, 2202089.
- 4 B. Pang, C. Liao, X. Xu, L. Yu, R. Li and Q. Peng, *Adv. Mater.*, 2023, **35**, 2300631.
- 5 J. Wan, Y. Wu, R. Sun, J. Qiao, X. Hao and J. Min, *Energy Environ. Sci.*, 2022, **15**, 5192-5201.
- 6 D. Li, N. Deng, Y. Fu, C. Guo, B. Zhou, L. Wang, J. Zhou, D. Liu, W. Li, K. Wang, Y. Sun and T. Wang, *Adv. Mater.*, 2023, **35**, 2208211.
- 7 Z. Zheng, J. Wang, P. Bi, J. Ren, Y. Wang, Y. Yang, X. Liu, S. Zhang and J. Hou, *Joule*, 2021, **1**, 171-184.
- 8 X. Wan, C. Li, M. Zhang and Y. Chen, *Chem. Soc. Rev.*, 2020, **49**, 2828-2842.
- 9 H. Yao and J. Hou, *Angew. Chem., Int. Ed.*, 2022, **37**, 202209021.
- 10 H. Liang, X. Bi, H. Chen, T. He, Y. Lin, Y. Zhang, K. Ma, W. Feng, Z. Ma, G. Long, C. Li, B. Kan, H. Zhang, O. A. Rakitin, X. Wan, Z. Yao and Y. Chen, *Nat. Commun.*, 2023, **14**, 4707.
- 11 W. Zhao, D. Qian, S. Zhang, S. Li, O. Inganäs, F. Gao and J. Hou, *Adv. Mater.*, 2016, **23**, 4734-4739.

- 12 K. Yoshikawa, H. Kawasaki, W. Yoshida, T. Irie, K. Konishi, K. Nakano, T. Uto, D. Adachi, M. Kanematsu, H. Uzu and K. Yamamoto, *Nat. Energy*, 2017, **2**, 17032.
- 13 Y. Tamai, *Adv. Energy Sustainability Res.*, 2022, **4**, 2200149.
- 14 J. Wang and X. Zhan, *Acc. Chem. Res.*, 2021, **54**, 132–143.
- 15 Y. Tong, Z. Xiao, X. Du, C. Zuo, Y. Li, M. Lv, Y. Yuan, C. Yi, F. Hao, Y. Hua, T. Lei, Q. Lin, K. Sun, D. Zhao, C. Duan, X. Shao, W. Li, H.-L. Yip, Z. Xiao, B. Zhang, Q. Bian, Y. Cheng, S. Liu, M. Cheng, Z. Jin, S. Yang and L. Ding, *Sci. China: Chem.*, 2020, **63**, 758–765.
- 16 Z. Luo, Y. Zhao, Z. G. Zhang, G. Li, K. Wu, D. Xie, W. Gao, Y. Li and C. Yang, *ACS Appl. Mater. Interfaces*, 2017, **39**, 34146–34152.
- 17 G. Zhang, F. R. Lin, F. Qi, T. Heumüller, A. Distler, H. J. Egelhaaf, N. Li, P. C. Y. Chow, C. J. Brabec, A. K. Jen and H. L. Yip, *Chem. Rev.*, 2022, **18**, 14180–14274.
- 18 L. Hong, H. Yao, Z. Wu, Y. Cui, T. Zhang, Y. Xu, R. Yu, Q. Liao, B. Gao, K. Xian, H. Y. Woo, Z. Ge and J. Hou, *Adv. Mater.*, 2019, **31**, 1903441.
- 19 S. Li, C.-Z. Li, M. Shi and H. Chen, *ACS Energy Lett.*, 2020, **5**, 1554–1567.
- 20 M. Deng, X. Xu, Y. Duan, L. Yu, R. Li and Q. Peng, *Adv. Mater.*, 2023, **35**, 2210760.
- 21 Y. Cui, H. Yao, J. Zhang, K. Xian, T. Zhang, L. Hong, Y. Wang, Y. Xu, K. Ma, C. An, C. He, Z. Wei, F. Gao and J. Hou, *Adv. Mater.*, 2020, **32**, 1908205.
- 22 C. Xiao, X. Wang, T. Zhong, R. Zhou, X. Zheng, Y. Liu, T. Hu, Y. Luo, F. Sun, B. Xiao, Z. Liu, C. Yang and R. Yang, *Adv. Sci.*, 2023, **7**, 2206580.
- 23 Q. Fan, R. Ma, J. Yang, J. Gao, H. Bai, W. Su, Z. Liang, Y. Wu, L. Tang, Y. Li, Q. Wu, K. Wang, L. Yan, R. Zhang, F. Gao, G. Li and W. Ma, *Angew. Chem., Int. Ed.*, 2023, **32**, 202308307.
- 24 K. Jiang, Q. Wei, J. Y. L. Lai, Z. Peng, H. K. Kim, J. Yuan, L. Ye, H. Ade, Y. Zou and H. Yan, *Joule*, 2019, **3**, 3020–3033.
- 25 J. Yuan, C. Zhang, H. Chen, C. Zhu, S. H. Cheung, B. Qiu, F. Cai, Q. Wei, W. Liu, H. Yin, R. Zhang, J. Zhang, Y. Liu, H. Zhang, W. Liu, H. Peng, J. Yang, L. Meng, F. Gao, S. So, Y. Li and Y. Zou, *Sci. China: Chem.*, 2020, **63**, 1159–1168.
- 26 C. Li, J. Zhou, J. Song, J. Xu, H. Zhang, X. Zhang, J. Guo, L. Zhu, D. Wei, G. Han, J. Min, Y. Zhang, Z. Xie, Y. Yi, H. Yan, F. Gao, F. Liu and Y. Sun, *Nat. Energy*, 2021, **6**, 605–613.
- 27 K. Chong, X. Xu, H. Meng, J. Xue, L. Yu, W. Ma and Q. Peng, *Adv. Mater.*, 2022, **13**, 2109516.
- 28 G. Chai, Y. Chang, Z. Peng, Y. Jia, X. Zou, D. Yu, H. Yu, Y. Chen, P. C. Y. Chow, K. S. Wong, J. Zhang, H. Ade, L. Yang and C. Zhan, *Nano Energy*, 2020, **76**, 105087.
- 29 J. Zhang, F. Bai, I. Angunawela, X. Xu, S. Luo, C. Li, G. Chai, H. Yu, Y. Chen, H. Hu, Z. Ma, H. Ade and H. Yan, *Adv. Energy Mater.*, 2021, **11**, 2102596.
- 30 Y. Chang, J. Zhang, Y. Chen, G. Chai, X. Xu, L. Yu, R. Ma, H. Yu, T. Liu, P. Liu, Q. Peng and H. Yan, *Adv. Energy Mater.*, 2021, **11**, 2100079.
- 31 G. Chai, Y. Chang, J. Zhang, X. Xu, L. Yu, X. Zou, X. Li, Y. Chen, S. Luo, B. Liu, F. Bai, Z. Luo, H. Yu, J. Liang, T. Liu, K. S. Wong, H. Zhou, Q. Peng and H. Yan, *Energy Environ. Sci.*, 2021, **14**, 3469–3479.
- 32 X. Kong, C. Zhu, J. Zhang, L. Meng, S. Qin, J. Zhang, J. Li, Z. Wei and Y. Li, *Energy Environ. Sci.*, 2022, **15**, 2011–2020.
- 33 Z. Li, C. Jiang, X. Chen, G. Song, X. Wan, B. Kan, T. Duan, E. A. Knyazeva, O. A. Rakitin and Y. Chen, *J. Mater. Chem. C*, 2023, **11**, 6920–6927.
- 34 L. J. A. Koster, V. D. Mihailetschi, R. Ramaker and P. W. M. Blom, *Appl. Phys. Lett.*, 2005, **86**, 123509.
- 35 S. R. Cowan, A. Roy and A. J. Heeger, *Phys. Rev. B: Condens. Matter Mater. Phys.*, 2010, **82**, 245207.
- 36 X. Zhang, C. Li, J. Xu, R. Wang, J. Song, H. Zhang, Y. Li, Y.-N. Jing, S. Li, G. Wu, J. Zhou, X. Li, Y. Zhang, X. Li, J. Zhang, C. Zhang, H. Zhou, Y. Sun and Y. Zhang, *Joule*, 2022, **6**, 444–457.
- 37 S. Nilsson, A. Bernasik, A. Budkowski and E. Moons, *Macromolecules*, 2007, **40**, 8291–8301.
- 38 Y. Yang, Z. G. Zhang, H. Bin, S. Chen, L. Gao, L. Xue, C. Yang and Y. Li, *J. Am. Chem. Soc.*, 2016, **138**, 15011–15018.
- 39 S. Liu, J. Yuan, W. Deng, M. Luo, Y. Xie, Q. Liang, Y. Zou, Z. He, H. Wu and Y. Cao, *Nat. Photonics*, 2020, **14**, 300–305.
- 40 T. Kirchartz and J. Nelson, *Phys. Rev. B: Condens. Matter Mater. Phys.*, 2012, **86**, 165201.
- 41 M. Kuik, L. J. A. Koster, G. A. H. Wetzelaer and P. W. M. Blom, *Phys. Rev. Lett.*, 2011, **107**, 256805.
- 42 T. Kirchartz, B. E. Pieters, J. Kirkpatrick, U. Rau and J. Nelson, *Phys. Rev. B: Condens. Matter Mater. Phys.*, 2011, **83**, 115209.